Fusion Engineering and Design 215 (2025) 114969

Contents lists available at ScienceDirect

Fusion Engineering and Design

journal homepage: www.elsevier.com/locate/fusengdes

Enabling model-based scenario control in EAST by fast surrogate modeling within COTSIM

Z. Wang [a,*], E. Schuster [a], T. Rafiq [a], Y. Huang [b], Z. Luo [b], Q. Yuan [c], J. Barr [c]

[a] Department of Mechanical Engineering and Mechanics, Lehigh University, Bethlehem, PA 18015, USA
[b] Institute of Plasma Physics, Chinese Academy of Sciences, Hefei 230031, PR China
[c] General Atomics, San Diego, CA 92121, USA

ARTICLE INFO

Keywords:
Transport modeling
Integrated tokamak simulation
Neural network model
EAST

ABSTRACT

The Control-Oriented Transport Simulator (COTSIM) is a fast, modular code designed to predict the evolution of both equilibrium and internal profiles in the EAST tokamak. Built on MATLAB/Simulink®, COTSIM is tailored for iterative control design, making it suitable for applications such as pulse design, feedforward scenario optimization, feedback-control testing prior to implementation, and real-time estimation and optimization. Recent advancements have enhanced its prediction accuracy for EAST while maintaining computational efficiency through the integration of neural-network-based surrogate models for the Multi-Mode Anomalous Transport Module (MMM), GENRAY/CQL3D (Lower Hybrid Wave [LHW]), and NUBEAM (Neutral Beam Injection [NBI]). Additionally, the transport solver has been coupled with both fixed-boundary and free-boundary equilibrium solvers. This study demonstrates the development and testing of model-based optimal feedback controllers in COTSIM simulations. These controllers regulate key plasma properties crucial for advanced tokamak scenarios, including the safety factor (q) at various spatial locations, plasma internal energy (W), normalized beta (β_N), and internal inductance (l_i). Control actuators include plasma current, plasma density, low-frequency (2.45 GHz) and high-frequency (4.60 GHz) LHW powers, and individual NBI powers. To validate these control algorithms, experimental testing has been conducted on EAST. Results from simulations and experiments demonstrate the ability to regulate scenario-defining plasma properties, suggesting COTSIM's utility as a tool for advanced tokamak control development.

1. Introduction

The pursuit of sustainable fusion energy has driven significant advancements in tokamak research. Understanding and controlling plasma behavior is critical for minimizing instabilities, maintaining confinement, and sustaining the conditions required for efficient and stable fusion reactions. Accurate and efficient simulation of plasma transport across various operating conditions plays a vital role in optimizing experimental operation and control strategies. Fast transport simulators are essential in this effort, enabling the rapid analysis of prior shots, providing insights into internal plasma states, and supporting between-shot planning. Moreover, they accelerate feedforward optimization, aid in training reinforcement learning algorithms for control strategies, and facilitate the design and implementation of model-based control systems.

Over the years, a variety of fast transport simulators have been developed to meet these needs. For example, METIS [1,2] enables rapid transport simulations by solving the current diffusion equation with scaling laws for resistivity and non-inductive currents, while estimating equilibrium using simplified analytic models or scaling laws. It is often used for preliminary scenario development and preparation for more comprehensive simulations like those conducted with CRONOS [3]. RAPTOR [4] provides real-time plasma profile evolution and is particularly useful for optimizing plasma operation scenarios [5] and performing sensitivity analysis [6] due to its differentiability. TORAX [7], a new open-source core transport simulator implemented in Python, provides fast runtimes and automatic differentiation, making it ideal for rapid scenario modeling, pulse design, and optimization of actuator trajectories. Other codes like ASTRA [8], TRANSP [9], and JINTRAC [10] offer higher-fidelity simulations but require significant computational time, making them suitable for detailed physics studies.

However, despite the advancements offered by these simulators, there is still a need for tools specifically designed for control applications that balance computational efficiency with sufficient accuracy and flexibility. Thus, the Control-Oriented Transport SIMulator (COT-

* Corresponding author.
E-mail address: zibo.wang@lehigh.edu (Z. Wang).

https://doi.org/10.1016/j.fusengdes.2025.114969
Received 14 January 2025; Received in revised form 10 March 2025; Accepted 11 March 2025
Available online 22 March 2025

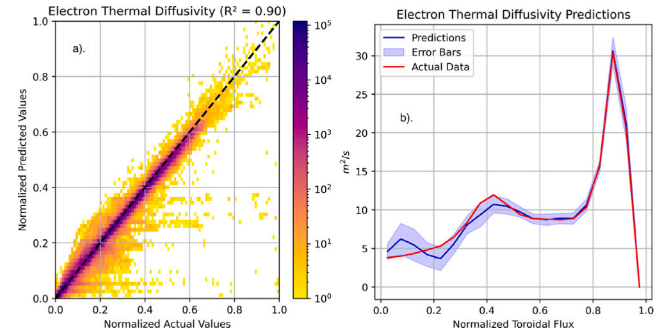

Fig. 1. Comparison of electron thermal diffusivity predictions between the MMMnet-lite surrogate model and the original MMM outputs. (a). Correlation plot showing the relationship between MMMnet-lite predictions and MMM outputs; (b). Spatial distribution of electron thermal diffusivity, with error bars representing the prediction variability at each spatial point.

SIM) [11] has been developed to address this gap. COTSIM is tailored for control-oriented applications, combining several key features that make it well-suited for control system design. These features include efficient execution for rapid scenario exploration and optimization, differentiability to enable advanced optimization techniques, and a modular and flexible design that allows for the selection of model complexity appropriate to the simulation needs, ensuring that essential dynamics are accurately captured. Furthermore, COTSIM employs a state-space representation [12] (i.e., a mathematical method describing system dynamics using first-order differential equations) for control system design and it allows implementations of advanced control algorithms such as model predictive control and reinforcement learning.

To achieve computational efficiency without compromising accuracy, COTSIM integrates multiple modeling approaches combining 1D physics-based transport equations with empirical models [13], confinement time scaling laws [14], and neural-network-based surrogate models for transport and sources [15–17]. This combination allows COTSIM to perform fast simulations while maintaining sufficient accuracy. Its modular structure supports ongoing development and customization, enabling integration with advanced physics models while retaining the computational speed needed for control system development and optimization. Furthermore, COTSIM offers flexibility by allowing the use of prescribed plasma equilibria or the coupling with fixed- and free-boundary equilibrium solvers [18–21]. These features make COTSIM ideal for between-shot analysis, feedback controller testing, and actuator trajectory optimization.

In this paper, fast neural network-based surrogate models are developed for NUBEAM, GENRAY, and the Multi-Mode Anomalous Transport Module (MMM) specifically for the EAST tokamak [22] and are integrated into COTSIM. With the integration of these surrogate models, COTSIM is utilized to predict the evolution of internal profiles in EAST. COTSIM takes inputs such as plasma current (I_p), line-averaged electron density ($\bar{n}_e$), and auxiliary heating and current drive (H&CD) sources. In this work, COTSIM solves the electron heat transport equation, the magnetic diffusion equation, and the toroidal rotation equation to predict the electron temperature, poloidal flux, and toroidal velocity profiles. COTSIM is utilized to develop and test model-based, optimal feedback controllers for critical plasma properties, such as the safety factor (q) profile, internal inductance (l_i), and normalized beta (β_N).

This paper is organized as follows. Section 2 covers the development and implementation of neural-network-based surrogate models for the EAST tokamak. Section 3 describes the physics-based models used in the version of COTSIM employed in this work, including plasma equilibrium, poloidal magnetic diffusion, and electron heat transport equations. Section 4 presents feedforward validation by comparing COTSIM simulations with experimental results. Section 5 provides feedback controller validation, also comparing COTSIM with experimental data. Finally, Section 6 concludes with a summary and future research directions.

2. Neural network surrogate models

Achieving high prediction accuracy of plasma parameters such as temperature, density, and current profiles, while significantly reducing computational requirements, is essential for enabling fast transport simulations. Previously, comprehensive neural network surrogate models [15,17,23] were developed for NUBEAM [24], GENRAY [25], and MMM [26,27], providing full predictive capabilities of their original codes. However, these surrogate models often entail substantial computational overhead, limiting their suitability for real-time applications. Thus, in this work, the above-mentioned limitation is addressed by developing three streamlined surrogate models optimized for fast execution within the COTSIM framework: NBInet-lite for NUBEAM, LHWnet-lite for GENRAY, and MMMnet-lite for MMM. Compared to the surrogate models presented in Refs. [15,17,23], which utilize the full input–output sets of the original codes, the network models developed in this work are designated with the suffix “lite” to reflect their reduced input requirements and simplified architectures, enabling rapid computations suitable for real-time applications. Each neural network-based surrogate model is specifically designed to capture the essential input–output relationships of its corresponding original code while maintaining a consistent architectural framework to facilitate development and integration into COTSIM. By focusing on the most critical aspects of the physical models, these “lite” versions achieve a balance between computational efficiency and predictive accuracy, making them highly suitable for integration into fast transport simulations and control systems. The inputs and outputs for each surrogate model are carefully selected and tailored to ensure compatibility with COTSIM and relevance to transport simulations. A sensitivity analysis [28] was employed to identify the most influential input parameters, systematically excluding variables with minimal impact on model predictions. Outputs, on the other hand, were chosen based on the specific requirements of transport simulations, directly reflecting the key plasma parameters necessary for accurate modeling. This approach ensures that surrogate models are both efficient to compute and relevant to practical simulation objectives within COTSIM. Table 1 summarizes the inputs and outputs for each surrogate model. By utilizing deep learning techniques, specifically multilayer perceptrons (MLPs), these surrogate models emulate the complex physics of the original codes (i.e., NUBEAM, GENRAY, MMM) while providing computations fast enough for integration into COTSIM for simulations. Each neural network is trained on a dataset generated by running the original codes over a wide range of plasma scenarios relevant to EAST operations. The range of Z_{eff} is from 1.5–2.5; the range of B_ϕ is from 2.3–3.5 T; the range of κ at plasma edge is from 1.6–2.4; the range of R is from 1.8–1.89 m; the range of a is from 0.45–0.5 m; the range of central electron temperature is from 0.5–5 keV; the range of central electron density is from 0.5–1 $\times$ 10^{19} m^{-3}; the range of q_{min} is 1.1–2.8; the range of Ω at plasma core is 0.47–2.6 $\times$ 10^5 rad/s; the range of $Vloop$ is from −1.1 to 2.1; and the range of P_{LH} and P_{NBI} are from 0–3 MW and 0–4 MW, respectively. Data preprocessing involves normalizing the input and output data to improve training stability and convergence. All networks employed the Gaussian Error Linear Unit (GELU) activation function in the hidden layers due to its proven performance in deep learning applications, especially for capturing nonlinear relationships. NBInet-lite (the surrogate model for NUBEAM) consists of four layers: an input layer, two hidden layers with GELU activations, and an output layer with a linear activation function. MMMnet-lite mirrors the structure of NBInet-lite and also has four layers and similar activation functions. LHWnet-lite (the surrogate model for GENRAY) comprises five layers: an input layer, three hidden layers with GELU activations

Table 1
Tailored input and output data of neural network-based surrogate models for efficient COTSIM computation.

	Descriptions	NBInet-lite	LHWnet-lite	MMMnet-lite
Inputs	Mean effective charge $Z_{\rm eff}$	✓	✓	✓
	Toroidal magnetic field B_ϕ	✓	✓	✓
	Elongation κ	✓		✓
	Major radius R	✓	✓	✓
	Minor radius a	✓		✓
	Electron density n_e	✓	✓	✓
	Electron temperature T_e	✓	✓	✓
	Safety factor profile q	✓	✓	✓
	Toroidal rotation Ω			✓
	Plasma loop voltage $Vloop$		✓	
	Lower hybrid wave power P_{LH}		✓	
	Neutral beam power P_{NBI}	✓		
Outputs	Power density deposition profile for NBI	✓		
	Power density deposition profile for LHW		✓	
	Current density deposition profile for NBI	✓		
	Current density deposition profile for LHW		✓	
	Electron thermal diffusivity χ_e			✓

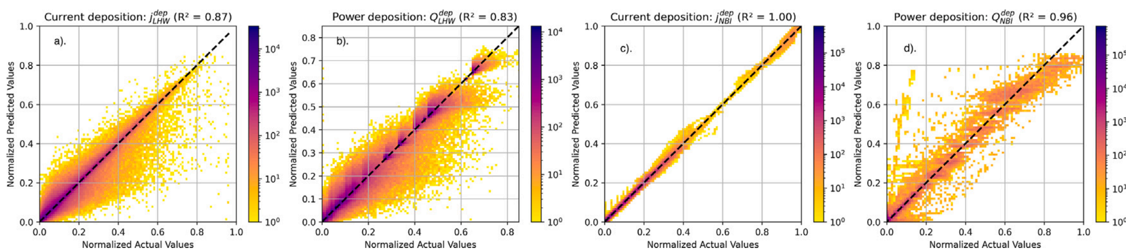

Fig. 2. Correlation plots comparing the predictions of the neural network surrogate models with the outputs of the original codes. (a) LHW current deposition predicted by LHWnet-lite versus GENRAY outputs; (b) LHW power deposition predicted by LHWnet-lite versus GENRAY outputs; (c) NBI current deposition predicted by NBInet-lite versus NUBEAM outputs; (d) NBI power deposition predicted by NBInet-lite versus NUBEAM outputs.

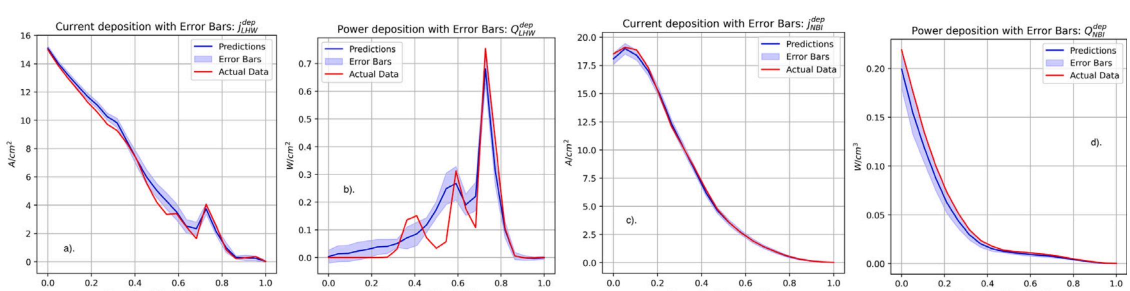

Fig. 3. Comparison of surrogate model predictions with original code outputs, with error bars representing the root mean square error (RMSE). (a) LHW current deposition profiles predicted by LHWnet-lite compared to GENRAY outputs; (b) LHW power deposition profiles predicted by LHWnet-lite compared to GENRAY outputs; (c) NBI current deposition profiles predicted by NBInet-lite compared to NUBEAM outputs; (d) NBI power deposition profiles predicted by NBInet-lite compared to NUBEAM outputs.

to address the complexity of the GENRAY surrogate problem, and an output layer with a linear activation function. The decision to use MLPs with these specific configurations is based on balancing model complexity and computational efficiency. The mean squared error (MSE) is used as the loss function to quantify the difference between the surrogate model predictions and the original code outputs. The Adam optimizer facilitates efficient gradient-based optimization during training.

The surrogate models are evaluated based on their ability to accurately replicate the outputs of the original codes while significantly reducing computation time. Correlation analysis shows high correlation coefficients between the surrogate model predictions and the original code outputs, indicating strong predictive performance. Comparative plots (Figs. 1–3) demonstrate excellent agreement between the neural network predictions and ground truth data across the range of scenarios tested. The surrogate models achieve speedups of several orders of magnitude compared to the original codes, with a prediction time of approximately 0.1 ms to simulate multiple plasma profiles for a single time slice, containing 101 radial points, on a personal computer. This high efficiency makes them suitable for real-time and iterative simulations within COTSIM.

3. Physical model

The geometry of the magnetic arrangement is depicted in Fig. 4, using a cylindrical coordinate system defined by (R, Z, ϕ) and magnetic-flux-surface-based coordinate system defined by (ρ, θ, ϕ). The helical magnetic field, $\mathbf{B}$, in a tokamak is composed of toroidal $\mathbf{B}_\phi$ and poloidal $\mathbf{B}_\theta$ components, i.e., $\mathbf{B} = \mathbf{B}_\phi + \mathbf{B}_\theta$. The poloidal magnetic flux at a point P within the tokamak, denoted by Ψ, is calculated as $\Psi \equiv \int_S \mathbf{B}_\theta \cdot d\mathbf{S}$. Here, S is a circular surface perpendicular to the Z-axis whose circumference passes through point P and $d\mathbf{S}$ is the differential surface vector. Regions of constant Ψ form nested surfaces. Critical plasma properties, including the safety factor, are constant on these flux surfaces. Thus, by adopting a spatial coordinate that indexes these nested surfaces and assuming axisymmetry, spatially varying plasma properties like the safety factor can be modeled as one-dimensional properties. In this work, the normalized mean effective minor radius,

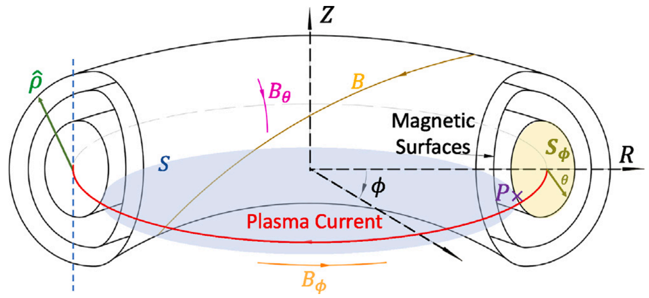

Fig. 4. Sketch of magnetic configuration. The poloidal ($\mathbf{B}_\theta$) and toroidal ($\mathbf{B}_\phi$) magnetic fields are combined to produce a helical magnetic field $\mathbf{B}$, which confines the plasma. In the poloidal plane (defined by the radial and vertical axes with coordinates R and Z, respectively), each point is identified by a value of the poloidal magnetic flux $\Psi(R, Z)$. Around the magnetic axis, points with identical $\Psi(R, Z)$ values define nested magnetic flux surfaces. Any quantity indexing these flux surfaces from the magnetic axis to the plasma boundary can be adopted as spatial coordinate ρ. The $\Psi(R, Z)$ is simplified as $\Psi(\hat{\rho}, \theta)$ with the assumption that the toroidal flux is axisymmetry in the toroidal coordinate.

defined as $\hat{\rho} \equiv \rho/\rho_b$, is used as the spatial coordinate. Here, ρ is defined as $\rho \equiv \sqrt{\Phi/(B_{\phi,0}\pi)}$, where $B_{\phi,0}$ is the vacuum toroidal magnetic field at the major radius R_0 and ρ_b is the value of ρ at the plasma edge. The toroidal magnetic flux, denoted by Φ, is given by $\Phi \equiv \int_{S_\phi} \mathbf{B}_\phi \cdot \mathrm{d}\mathbf{S}_\phi$, where S_ϕ is a surface perpendicular to the ϕ-axis whose boundary includes point P and $d\mathbf{S}_\phi$ is the differential surface vector normal to S_ϕ.

3.1. MHD equilibrium

Building upon the magnetic geometry in tokamaks, plasma equilibrium is achieved when the pressure gradient within the plasma is exactly balanced by the magnetic forces arising from the plasma current and confining magnetic fields. This balance ensures that the plasma remains confined within the desired region. The theoretical framework for describing this balance is provided by magnetohydrodynamics (MHD), which combines principles from both fluid dynamics and electromagnetism.

The MHD equilibrium equations are derived from three fundamental principles: the conservation of magnetic flux ($\nabla \cdot \mathbf{B} = 0$), Ampère's law ($\nabla \times \mathbf{B} = \mu_0 \mathbf{J}$), and the force balance condition ($\mathbf{J} \times \mathbf{B} = \nabla p$), where $\mathbf{J}$ is the current density, p is the plasma pressure, and μ_0 is the permeability of free space. By assuming axisymmetry, it leads to the Grad–Shafranov equation [29,30], which encapsulates the magnetic field configuration and plasma pressure distribution:

$$\Delta^* \psi(R, Z) = R \frac{\partial p}{\partial \psi} + \frac{f}{\mu_0 R} \frac{\partial f}{\partial \psi}, \tag{1}$$

where $p(\psi)$ is plasma kinetic pressure, f is the diamagnetic function $f(\psi) \equiv R B_\phi$, and the operator Δ^* is defined as

$$\Delta^* \equiv R \frac{\partial}{\partial R}\left(\frac{1}{R}\frac{\partial}{\partial R}\right) + \frac{\partial^2}{\partial Z^2}. \tag{2}$$

Several methods are employed in COTSIM to solve the Grad–Shafranov equation. Specifically, three fixed-boundary equilibrium solvers have been implemented [18–20], providing flexibility and accuracy in modeling plasma equilibria under prescribed boundary conditions. Recently, new free-boundary equilibrium solvers have been coupled into COTSIM [16,21], enabling simulations where the plasma boundary can evolve dynamically in response to internal and external conditions.

3.2. Current density and safety factor profile

The current density profile within a tokamak plasma is a fundamental aspect that significantly influences plasma behavior, stability, and performance. In transport codes used for simulating tokamak plasmas, accurately modeling the current profile is crucial because it directly affects the magnetic configuration and the evolution of key plasma parameters. The evolution of the current density profile is governed by the Magnetic Diffusion Equation (MDE), which describes how the poloidal magnetic flux diffuses through the plasma over time. The MDE is derived from Maxwell's equations and Ohm's law under the assumptions of axisymmetry and cylindrical geometry. In this framework, the stream function ψ represents the poloidal flux per radian inside the major radius R. The MDE dictates the evolution of the stream function and takes the form:

$$\frac{\partial \psi}{\partial t} = \frac{\eta}{\mu_0 \rho_b^2 \hat{F}^2} \frac{1}{\hat{\rho}} \frac{\partial}{\partial \hat{\rho}} \left(\hat{\rho} D_\psi \frac{\partial \psi}{\partial \hat{\rho}} \right) + R_0 \hat{H} \eta \frac{\langle \mathbf{j}_{NI} \cdot \mathbf{B} \rangle}{B_{\phi,0}}, \tag{3}$$

subject to the boundary conditions

$$\frac{\partial \psi}{\partial \hat{\rho}}\Big|_{\hat{\rho}=0} = 0, \qquad \frac{\partial \psi}{\partial \hat{\rho}}\Big|_{\hat{\rho}=1} = k_{I_p} I_p, \tag{4}$$

where I_p is the plasma current, η is the plasma resistivity, T_e is the electron temperature. The parameters $\hat{F}$, $\hat{G}$, and $\hat{H}$ are geometric factors [13] capturing the topology of the MHD equilibrium. Users have the option to compute these factors using a prescribed plasma equilibrium, the fixed boundary solvers [18–20], or the free boundary solver [21]. The notation $\langle \cdot \rangle$ is used to denote the flux-surface average of a quantity. The terms D_ψ in and k_{I_p} are defined as $D_\psi(\hat{\rho}) \triangleq \hat{F}(\hat{\rho})\hat{H}(\hat{\rho})\hat{G}(\hat{\rho})$ and $k_{I_p} \triangleq -\frac{\mu_0}{2\pi}\frac{R_0}{\hat{G}(1)\hat{H}(1)}$. The non-inductive current drive ($\mathbf{j}_{NI}$) is the sum of the self-generated bootstrap current ($\mathbf{j}_{BS}$) and each of the auxiliary sources such as lower hybrid wave ($\mathbf{j}_{lhw}$) and neutral beam injection ($\mathbf{j}_{nbi}$),

$$\frac{\langle \mathbf{j}_{NI} \cdot \mathbf{B} \rangle}{B_{\phi,0}} = \sum_{i=1}^{n_{nbi}} \frac{\langle \mathbf{j}_{nbi_i} \cdot \mathbf{B} \rangle}{B_{\phi,0}} + \sum_{l=1}^{n_{lhw}} \frac{\langle \mathbf{j}_{lhw_l} \cdot \mathbf{B} \rangle}{B_{\phi,0}} + \frac{\langle \mathbf{j}_{BS} \cdot \mathbf{B} \rangle}{B_{\phi,0}}, \tag{5}$$

where n_{nbi} and n_{lhw} are the number of NBI and LHW sources, respectively. The EAST tokamak is equipped with 4 NBIs and 2 LHWs. The values $\mathbf{j}_{nbi}$ and $\mathbf{j}_{lhw}$ can be obtained from the NN-based surrogate as shown in Section 2, or by parameterized empirical laws [31]. The bootstrap current model is based on [32], which after incorporating the electron-ion tight coupling assumption reduces to

$$\frac{\langle \mathbf{j}_{BS} \cdot \mathbf{B} \rangle}{B_{\phi,0}}(\hat{\rho}, t) = \frac{R_0}{\hat{F}\left(\frac{\partial \psi}{\partial \hat{\rho}}\right)} \left[\mathcal{L}_1 T_e \frac{\partial n_e}{\partial \hat{\rho}} + \mathcal{L}_2 n_e \frac{\partial T_e}{\partial \hat{\rho}} \right], \tag{6}$$

where the spatial functions $\mathcal{L}_1(\hat{\rho})$ and $\mathcal{L}_2(\hat{\rho})$ depend on the magnetic configuration of the MHD equilibrium. Finally, the plasma resistivity follows the Spitzer model.

The q profile at location $\hat{\rho}$ and time t is defined as

$$q(\hat{\rho}, t) = -B_{\phi,0} \rho_b^2 \hat{\rho} \left(\frac{\partial \psi}{\partial \hat{\rho}} \right)^{-1}, \tag{7}$$

where ψ is the poloidal stream function defined as $\psi \triangleq \Psi/2\pi$. Thus, the q profile can be regulated by controlling the gradient of the stream function.

3.3. Electron heat transport equation

As evident from Eq. (3), the evolution of ψ depends on the evolution of the electron temperature T_e. When heat diffusion is the dominant transport mechanism, the evolution of T_e can be modeled using the electron heat transfer equation (EHTE), which can be expressed as

$$\frac{3}{2} \frac{\partial}{\partial t} \left[n_e T_e \right] = \frac{1}{\rho_b^2 \hat{H}} \frac{1}{\hat{\rho}} \frac{\partial}{\partial \hat{\rho}} \left[\hat{\rho} \frac{\hat{G}\hat{H}^2}{\hat{F}} \left(\chi_e n_e \frac{\partial T_e}{\partial \hat{\rho}} \right) \right] + Q_e, \tag{8}$$

with the boundary conditions

$$\frac{\partial T_e}{\partial \hat{\rho}}\Big|_{\hat{\rho}=0} = 0, \qquad T_e(1, t) = T_{e,bdry}(t), \tag{9}$$

where $T_{e,bdry}$ is the temperature at the plasma edge. The electron thermal diffusivity $\chi_e(\hat{\rho}, t)$ can be computed by different physics-based models such as Bohm/gyro–Bohm model [33], or neural network-based surrogate models. The total electron heating power density is denoted as $Q_e(\hat{\rho}, t)$, which is expressed as

$$Q_e(\hat{\rho}, t) = Q_{ohm}(\hat{\rho}, t) + \sum_{i=1}^{n_{aux}} Q_{aux_i}(\hat{\rho}, t) - Q_{rad}(\hat{\rho}, t), \quad (10)$$

where Q_{ohm} is the ohmic power density, Q_{rad} is the radiation power density, Q_{aux} is the auxiliary power density, and Q_{fus} is the fusion power (which is non-zero in the case of burning plasmas). The fusion power is usually multiplied by a coefficient η_{fus} that represents the effectiveness of the fusion reaction in heating the plasma. The auxiliary power density is computed by

$$Q_{aux} \triangleq Q_{NBI} + Q_{LH} = \sum_{i=1}^{n_{nbi}} Q_{NBI_i}(t) + \sum_{i=1}^{n_{lhw}} Q_{LH_i}(t),$$

where Q_{NBI} and Q_{LH} are neutral beam injection and lower hybrid wave heating profiles, respectively. The values of Q_{NBI} and Q_{LH} can either be calculated by empirical model [31] or be predicted by neural network-based surrogate models introduced in Section 2. The evolution of the electron density n_e is modeled in this work as

$$n_e(\hat{\rho}, t) = n_e^{prof}(\hat{\rho})\bar{n}_e(t), \quad (11)$$

where n_e^{prof} is a reference electron density profile and $\bar{n}_e$ is the line average electron density. It is worth mentioning that, given the plasma conditions in this study, it is reasonable to assume strong electron-ion coupling, allowing the simplification $T_i = T_e$. Additionally, assuming a fully ionized, single-species, hydrogenic plasma, quasi-neutrality implies $n_i = n_e$.

4. COTSIM validation: Feedforward simulations

The performance and accuracy of COTSIM are validated through a comparative study with TRANSP simulations, using experimental data from EAST discharge #128 474. To ensure that the equilibrium conditions in simulations closely match those observed experimentally, both TRANSP and COTSIM utilize the same EFIT data. Specifically, TRANSP takes the equilibrium profiles directly from EFIT, while COTSIM uses the boundary conditions extracted from the same EFIT data in its fixed-boundary equilibrium solver. The simulation inputs included the plasma current and auxiliary heating and current drive (H&CD) sources, specifically neutral beam injections NBI2 and NBI4, and 4.6 GHz lower hybrid wave. The actuator waveforms for inputs are presented in Fig. 5, aligning with the actual operational settings of the experimental discharge. Both simulations use the same transport models for sources and transport processes to ensure meaningful comparisons. TRANSP employs the full physics models NUBEAM, GENRAY, and MMM to simulate neutral beam injection, radio frequency wave propagation, and anomalous transport, respectively. Meanwhile, COTSIM utilizes the corresponding surrogate models NBInet-lite, LHWnet-lite, and MMMnet-lite for rapid computations. Additionally, the magnetic diffusion equation is solved using a hybrid solver, which combines explicit and implicit numerical methods, on a spatial grid of 101 points. It efficiently computes the evolution of the poloidal magnetic flux, which is crucial for determining the current density profile and the q profile.

The results of the q-profile simulation at normalized radial positions 0.1, 0.5, and 0.9 are shown in Fig. 5. The mean squared errors (MSE) between the COTSIM and TRANSP q-profiles are 0.0065 at $\hat{\rho} = 0.1$, 0.007 at $\hat{\rho} = 0.5$, and 0.024 at $\hat{\rho} = 0.9$. The larger MSE at the boundary is primarily due to the higher absolute values of q in this region, which naturally result in larger squared differences. Despite the small biases in the predictions, the low MSE values indicate good agreement between the simulations. These slight differences are likely due to variations in the plasma equilibrium assumptions between COTSIM and TRANSP. Specifically, COTSIM assumes fixed boundary conditions for the equilibrium, while TRANSP uses EFIT data to determine the equilibrium. The exact cause of these biases is still under investigation, but differences in equilibrium assumptions remain a possible explanation. These small biases are considered relatively irrelevant in the context of feedback control applications, where controllers are designed with integral components to compensate for such biases. However, the biases may affect feedforward control applications such as scenario optimization in spite of their small magnitude, which justifies present efforts towards understanding the exact cause of these biases.

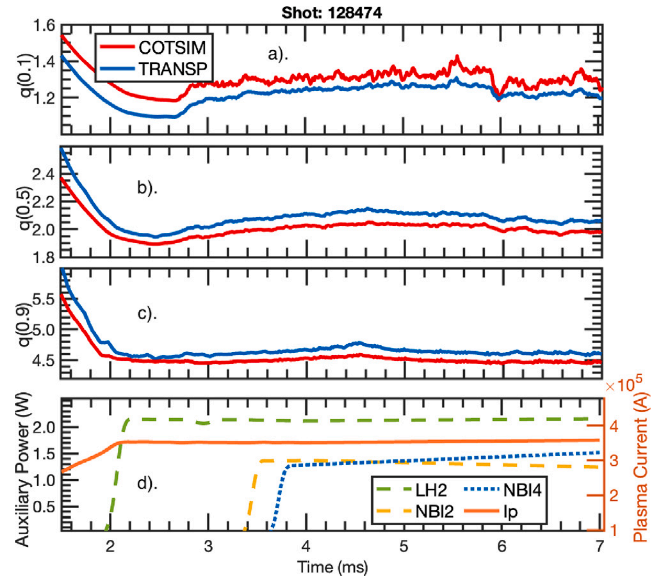

Fig. 5. Comparison of q-profile evolution between COTSIM and TRANSP simulations, along with actuator waveforms for shot #128 474: (a) q at $\hat{\rho} = 0.1$; (b) q at $\hat{\rho} = 0.5$; (c) q at $\hat{\rho} = 0.9$; (d) I_p and auxiliary power inputs.

5. Validation of Feedforward + Feedback control simulations

To validate the capabilities of COTSIM and demonstrate its applicability for testing control strategies and feedforward optimization, a series of experiments were conducted on the EAST tokamak involving both feedforward-only and combined feedforward and feedback control schemes. The feedback controllers tested in this work are Linear Quadratic Integral (LQI) controllers, as previously published in [34].

The first set of experiments focused on the regulation of the q profile. To establish a baseline, an initial feedforward-only discharge, shot #103 719, was executed using predetermined inputs for plasma current (I_p) and 4.6 GHz lower hybrid wave power. This shot provided reference data for plasma behavior without feedback control. Subsequently, to generate feasible target evolutions for the q profile, a second feedforward-only shot, discharge #103 720, was performed with a different set of input waveforms compared to shot #103 719. The q profile obtained from this shot served as the target profile for the feedback control experiment. The feedforward-feedback shot #103 737 used the same feedforward inputs as shot #103 719, with the LQI controller actively adjusting inputs to track the target q profile from shot #103 720. In this feedback-controlled experiment, the controller actively modified only the plasma current I_p and the lower hybrid wave power P_{LH2}, sending requests within predefined operational ranges of $I_p \in [0.3, 0.6]$ MA and $P_{LH2} \in [1.0, 2.9]$ MW to ensure safe and feasible operation. The controller was set to activate at 2 s. As shown in Fig. 6, the controller effectively regulated the evolution of the q-profile at different radial positions, following predefined target trajectories. At the outer radius ($\hat{\rho} = 0.9$), the target q-profile exhibited a trapezoidal shape, clearly designed to test the controller by requiring

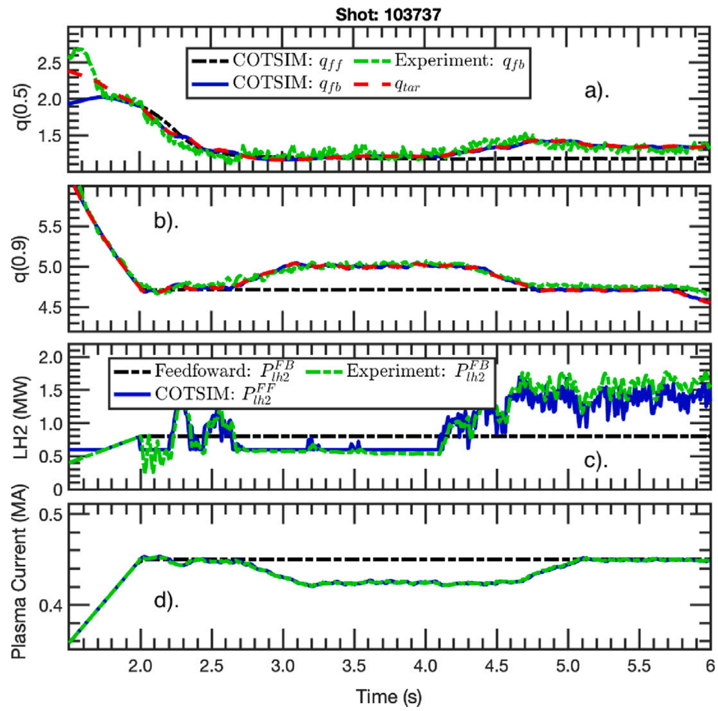

Fig. 6. Comparison of q-profile evolution between COTSIM and TRANSP simulations and actuator waveforms for shot #103 737: (a) q at $\hat{\rho} = 0.5$; (b) q at $\hat{\rho} = 0.9$; (c) Lower hybrid power; (d) Plasma current. The black dot-dashed lines represent trajectories from shot #103 719, the blue dot-dashed lines correspond to trajectories from shot #103 737, the blue solid lines show simulation results from COTSIM, and the red dashed lines indicate the target trajectories generated from shot #103 720.

specific manipulations of the plasma current I_p. Initially, from about 2.7 s, I_p began decreasing to achieve the increasing phase of the $q(0.9)$ target trajectory. Subsequently, $q(0.9)$ reached a plateau around 3.2 s, during which I_p remained nearly constant. After this flat phase, starting from around 4.7 s, the target $q(0.9)$ decreased, requiring an increase in I_p. Finally, $q(0.9)$ stabilized again as the plasma current leveled off towards the end of the discharge. Meanwhile, at mid-radius ($\hat{\rho} = 0.5$), the control of the q-profile was predominantly influenced by the auxiliary lower hybrid power (P_{LH2}). A clear adjustment in P_{LH2} occurred around 4.1 s, coinciding with the target increase in $q(0.5)$. This resulted in a noticeable rise in P_{LH2} to effectively track the targeted profile. These deliberate actuator manipulations clearly demonstrate the controller's capability to independently regulate plasma parameters at different radial positions. Meanwhile, both the COTSIM simulations and the experimental results exhibited similar behavior, confirming that COTSIM accurately models the plasma response under feedback control conditions. This successful regulation of the q profile highlights the effectiveness of the LQI controller and validates the use of COTSIM for controller testing and feedforward optimization.

The second set of experiments assessed the controller's ability to simultaneously regulate the internal inductance (l_i) and the normalized beta (β_N). Initially, a feedforward-only shot, discharge #114 107, was executed to serve as a baseline, providing reference data without feedback intervention. To obtain feasible target evolutions for l_i and β_N, another feedforward-only shot, discharge #114 106, was performed with input settings different from those used in shot #114 107. The trajectories of l_i and β_N from this shot were used as the target trajectories for the subsequent feedback control experiment. The feedforward plus feedback controlled shot, discharge #114 120, was then conducted using the same feedforward inputs as in shot #114 107 but with the LQI controller adjusting the inputs to track the target l_i and β_N trajectories obtained from shot #114 106. The controller was engaged at 2 s. As shown in Fig. 7, COTSIM simulations demonstrated consistent tracking of both l_i and β_N after the controller was turned on, closely following the target trajectories. In the experiment, however, β_N and l_i took

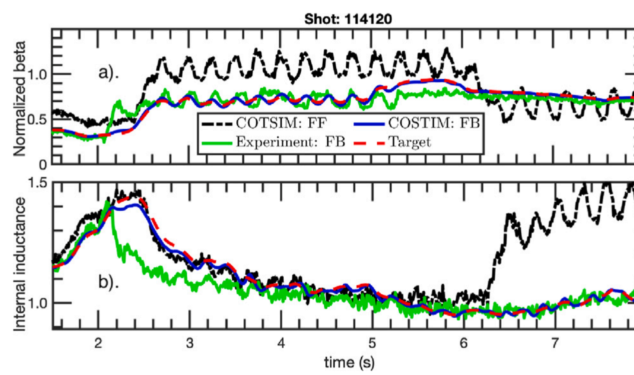

Fig. 7. Comparison of β_N and l_i evolution between COTSIM and TRANSP simulations for EAST discharge #114 120: (a) Feedback simulation and experimental results for β_N. (b) Feedback simulation and experimental results for l_i. The black dot-dashed lines represent the feedforward trajectory from shot #114 106, the blue solid lines correspond to the COTSIM feedback simulation, the green solid lines show the experimental results from shot #114 120, and the red dashed lines indicate the target trajectory from shot #114 107.

longer to align with the target, with β_N reaching effective tracking after approximately 0.5 s and l_i after 2 s. Despite these initial discrepancies, both parameters eventually converged to the target, achieving a similar tracking performance as observed in the simulations. This alignment between COTSIM simulations and experimental results in regulating both l_i and β_N highlights COTSIM's effectiveness in modeling plasma behavior under feedback control. These findings demonstrate that COTSIM can serve as a valuable tool for testing and optimizing control algorithms prior to their implementation in actual tokamak operations. By accurately replicating the plasma response to control inputs, COTSIM could be used to refine controller designs, reduce risks associated with experimental trials, and enhance the efficiency of experimental campaigns.

6. Conclusions and future work

This work presents further development of the Control-Oriented Transport SIMulator (COTSIM), designed to deliver high predictive accuracy with significantly reduced computational requirements by leveraging neural network-based surrogate models. The accuracy of COTSIM predictions is validated through comparisons with TRANSP simulations and experimental data from the EAST tokamak. COTSIM demonstrates qualitative agreement with TRANSP in predicting the evolution of critical plasma parameters, including the safety factor, internal inductance, and normalized beta. Regulation experiments using LQI controllers highlight COTSIM's ability to accurately replicate the plasma response to real-time control adjustments, reinforcing its utility as a tool for control algorithm testing and optimization. COTSIM's computational efficiency offers distinct advantages for between-shot planning, feedforward optimization, and iterative control strategy development. By enabling rapid, high-fidelity simulations that closely mirror experimental outcomes, COTSIM reduces risks associated with experimental trials and enhances the efficiency of experimental campaigns.

Future work will focus on further enhancing the accuracy of the surrogate models and expanding their applicability to a wider range of plasma conditions. Planned developments include integrating additional transport equations, such as ion heat and particle transport equations, to improve simulation fidelity. Additionally, different optimization schemes coupling transport and free-boundary equilibrium solvers will be studied to enable simultaneous shape and profile optimization over the duration of the discharge. These developments will further extend COTSIM's capabilities, strengthening its applicability in advanced control design, scenario planning, and real-time tokamak operation.

CRediT authorship contribution statement

Z. Wang: Writing – original draft, Visualization, Software, Methodology. **E. Schuster:** Writing – review & editing, Software, Methodology, Funding acquisition, Conceptualization. **T. Rafiq:** Writing – review & editing, Methodology. **Y. Huang:** Resources, Data curation. **Z. Luo:** Resources, Data curation. **Q. Yuan:** Software, Resources. **J. Barr:** Resources.

Declaration of competing interest

The authors declare that they have no known competing financial interests or personal relationships that could have appeared to influence the work reported in this paper.

Acknowledgments

This material is based upon work supported by the U.S. Department of Energy, Office of Science, Office of Fusion Energy Sciences (FES), under Award Number DE-SC0010537.

Data availability

Data will be made available on request.

References

[1] J. Artaud, F. Imbeaux, J. Garcia, G. Giruzzi, T. Aniel, V. Basiuk, A. Bécoulet, C. Bourdelle, Y. Buravand, J. Decker, et al., METIS: a fast integrated tokamak modelling tool for scenario design, Nucl. Fusion 58 (10) (2018) 105001.

[2] Y. Tao, M. Li, J. Qian, D. Moreau, B. Zhang, H. Xu, W. Xu, P. Li, X. Yang, W. Liu, et al., Simulation of current density profile for EAST advanced scenario with METIS code, Fusion Eng. Des. 200 (2024) 114177.

[3] J. Artaud, V. Basiuk, F. Imbeaux, M. Schneider, J. Garcia, G. Giruzzi, P. Huynh, T. Aniel, F. Albajar, J. Ané, et al., The CRONOS suite of codes for integrated tokamak modelling, Nucl. Fusion 50 (4) (2010) 043001.

[4] F. Felici, J. Citrin, A. Teplukhina, J. Redondo, C. Bourdelle, F. Imbeaux, O. Sauter, J. Contributors, E.M. Team, et al., Real-time-capable prediction of temperature and density profiles in a tokamak using RAPTOR and a first-principle-based transport model, Nucl. Fusion 58 (9) (2018) 096006.

[5] S. Van Mulders, Full-Discharge Simulation and Optimization with the RAPTOR Code, from Present Tokamaks to ITER and DEMO, Tech. Rep., EPFL, 2023.

[6] S. Van Mulders, F. Felici, O. Sauter, J. Citrin, A. Ho, M. Marin, K. Van de Plassche, Rapid optimization of stationary tokamak plasmas in RAPTOR: demonstration for the ITER hybrid scenario with neural network surrogate transport model QLKNN, Nucl. Fusion 61 (8) (2021) 086019.

[7] J. Citrin, I. Goodfellow, A. Raju, J. Chen, J. Degrave, C. Donner, F. Felici, P. Hamel, A. Huber, D. Nikulin, et al., TORAX: A fast and differentiable tokamak transport simulator in JAX, 2024, arXiv preprint arXiv:2406.06718.

[8] G.V. Pereverzev, P. Yushmanov, ASTRA. Automated System for Transport Analysis in a Tokamak, Tech. Rep., Max-Planck-Institut für Plasmaphysik, 2002.

[9] B. Grierson, X. Yuan, M. Gorelenkova, S. Kaye, N. Logan, O. Meneghini, S. Haskey, J. Buchanan, M. Fitzgerald, S. Smith, et al., Orchestrating TRANSP simulations for interpretative and predictive tokamak modeling with OMFIT, Fusion Sci. Technol. 74 (1–2) (2018) 101–115.

[10] M. Romanelli, G. Corrigan, V. Parail, S. Wiesen, R. Ambrosino, P.D.S.A. Belo, L. Garzotti, D. Harting, F. Koechl, T. Koskela, et al., JINTRAC: a system of codes for integrated simulation of tokamak scenarios, Plasma Fusion Res. 9 (2014) 3403023–3403023.

[11] A. Pajares, E. Schuster, Current profile and normalized beta control via feedback linearization and Lyapunov techniques, Nucl. Fusion 61 (3) (2021) 036006.

[12] R.L. Williams, D.A. Lawrence, et al., Linear State-Space Control Systems, John Wiley & Sons, 2007.

[13] Y. Ou, T. Luce, E. Schuster, J. Ferron, M. Walker, C. Xu, D. Humphreys, Towards model-based current profile control at DIII-D, Fusion Eng. Des. 82 (5–14) (2007) 1153–1160.

[14] R.J. Goldston, Energy confinement scaling in tokamaks: some implications of recent experiments with ohmic and strong auxiliary heating, Plasma Phys. Control. Fusion 26 (1A) (1984) 87.

[15] Z. Wang, S. Morosohk, T. Rafiq, E. Schuster, M.D. Boyer, W. Choi, Neural network model of neutral beam injection in the EAST tokamak to enable fast transport simulations, Fusion Eng. Des. 191 (2023) 113514.

[16] Z. Wang, X. Song, T. Rafiq, E. Schuster, Neural-network-based free-boundary equilibrium solver to enable fast scenario simulations, IEEE Trans. Plasma Sci. (2024) 1–7.

[17] G. Wallace, Z. Bai, R. Sadre, T. Perciano, N. Bertelli, S. Shiraiwa, E. Bethel, J. Wright, Towards fast and accurate predictions of radio frequency power deposition and current profile via data-driven modelling: applications to lower hybrid current drive, J. Plasma Phys. 88 (4) (2022) 895880401.

[18] S. Zheng, A. Wootton, E.R. Solano, Analytical tokamak equilibrium for shaped plasmas, Phys. Plasmas 3 (3) (1996) 1176–1178.

[19] A.J. Cerfon, J.P. Freidberg, "One size fits all" analytic solutions to the Grad–Shafranov equation, Phys. Plasmas 17 (3) (2010).

[20] Y.M. Jeon, Development of a free-boundary tokamak equilibrium solver for advanced study of tokamak equilibria, J. Korean Phys. Soc. 67 (2015) 843–853.

[21] X. Song, B. Leard, Z. Wang, S.T. Paruchuri, T. Rafiq, E. Schuster, Control-oriented free-boundary equilibrium solver for tokamaks, Plasma 7 (4) (2024) 842–857.

[22] S. Wu, E. team, et al., An overview of the EAST project, Fusion Eng. Des. 82 (5–14) (2007) 463–471.

[23] S. Morosohk, A. Pajares, T. Rafiq, E. Schuster, Neural network model of the multi-mode anomalous transport module for accelerated transport simulations, Nucl. Fusion 61 (10) (2021) 106040.

[24] A. Pankin, D. McCune, R. Andre, G. Bateman, A. Kritz, The tokamak Monte Carlo fast ion module NUBEAM in the National Transport Code Collaboration library, Comput. Phys. Comm. 159 (3) (2004) 157–184.

[25] A. Smirnov, R. Harvey, The GENRAY ray tracing code, CompX Rep. CompX-2000- 01 (2001).

[26] T. Rafiq, A. Kritz, J. Weiland, A. Pankin, L. Luo, Physics basis of multi-mode anomalous transport module, Phys. Plasmas 20 (3) (2013) 032506.

[27] L. Luo, T. Rafiq, A. Kritz, Improved multi-mode anomalous transport module for tokamak plasmas, Comput. Phys. Comm. 184 (10) (2013) 2267–2276.

[28] A. Saltelli, M. Ratto, T. Andres, F. Campolongo, J. Cariboni, D. Gatelli, M. Saisana, S. Tarantola, Global Sensitivity Analysis: the Primer, John Wiley & Sons, 2008.

[29] V. Shafranov, On magnetohydrodynamical equilibrium configurations, Sov. Phys. JETP 6 (3) (1958) 1013.

[30] H. Grad, H. Rubin, Hydromagnetic equilibria and force-free fields, J. Nucl. Energy (1954) 7 (3–4) (1958) 284–285.

[31] Z. Wang, E. Schuster, T. Rafiq, Y. Huang, Z. Luo, Q. Yuan, B. Xiao, D. Humphreys, Refinement of control-oriented model via TRANSP-based transport analysis to enable systematic model-based scenario planning in EAST, in: APS Division of Plasma Physics Meeting Abstracts, Vol. 2021, 2021, pp. TP11–112.

[32] O. Sauter, C. Angioni, Y. Lin-Liu, Neoclassical conductivity and bootstrap current formulas for general axisymmetric equilibria and arbitrary collisionality regime, Phys. Plasmas 6 (7) (1999) 2834–2839.

[33] M. Erba, T. Aniel, V. Basiuk, A. Becoulet, X. Litaudon, Validation of a new mixed Bohm/gyro-Bohm model for electron and ion heat transport against the ITER, Tore Supra and START database discharges, Nucl. Fusion 38 (7) (1998) 1013.

[34] Z. Wang, H. Wang, E. Schuster, Z. Luo, Y. Huang, Q. Yuan, B. Xiao, D. Humphreys, Optimal shaping of the safety factor profile in the EAST Tokamak, in: 2021 IEEE Conference on Control Technology and Applications, CCTA, IEEE, 2021, pp. 63–68.